



Swansea University
Prifysgol Abertawe



Cronfa - Swansea University Open Access Repository

This is an author produced version of a paper published in :
Nature Geoscience

Cronfa URL for this paper:
<http://cronfa.swan.ac.uk/Record/cronfa22721>

Paper:

James, T., Murray, T., Selmes, N., Scharrer, K. & O'Leary, M. Buoyant flexure and basal crevassing in dynamic mass loss at Helheim Glacier. *Nature Geoscience*, 7(8), 593-596.

<http://dx.doi.org/10.1038/ngeo2204>

This article is brought to you by Swansea University. Any person downloading material is agreeing to abide by the terms of the repository licence. Authors are personally responsible for adhering to publisher restrictions or conditions. When uploading content they are required to comply with their publisher agreement and the SHERPA RoMEO database to judge whether or not it is copyright safe to add this version of the paper to this repository.

<http://www.swansea.ac.uk/iss/researchsupport/cronfa-support/>

1 **Buoyant flexure controls summer dynamic mass loss at Helheim**

2 **Glacier, Greenland**

3

4 Timothy D. James*, Tavi Murray, Nick Selmes, Kilian Scharrer and Martin O’Leary

5 *Glaciology Group, Department of Geography, Swansea University, Singleton Park, Swansea,*

6 *SA2 8PP, United Kingdom*

7

8 Corresponding author T.D. James (t.d.james@swansea.ac.uk)

9

10

11 **Iceberg calving accounts for a significant proportion of annual mass loss from**
12 **tidewater-terminating glaciers^{1,2} and was likely a major factor in the rapid demise of**
13 **paleo-ice sheets³. Recent forecasts of sea-level contributions from the main outlet**
14 **glaciers of the Greenland Ice Sheet find the majority of mass-loss will be dynamic in**
15 **origin over the next two centuries⁴. However, despite the use of increasingly realistic,**
16 **physically-based approaches for representing the important calving component, current**
17 **models remain a coarse approximation of real calving mechanisms. This is due largely**
18 **to a lack of observational data of glacier geometry required for the development of 3D**
19 **time-evolving models⁵. Here we present a high temporal and spatial resolution record of**
20 **daily digital elevation models (DEMs) of the calving margin of Greenland's Helheim**
21 **Glacier during the summers of 2010 and 2011 derived from stereo terrestrial**
22 **photography. Our results show that during these summers large (>1 km³) calving events**
23 **driven by buoyant flexure dominated dynamic mass loss at Helheim. This calving**
24 **mechanism, common at Helheim and likely elsewhere in Greenland, is clearly an**
25 **important first-order control on the ice sheet's mass balance. However, recent models**
26 **favour surface-driven crevasse propagation as the first-order control on calving and**
27 **thus could be misrepresenting dynamic mass-loss from the ice sheet.**

28 A widely adopted approach for representing calving in glacier and ice sheet models due to its
29 ability to simulate a wide variety of calving behaviour is to define calving front location as
30 the point where transverse surface crevasses propagate to the waterline¹¹. Although a
31 simplification, crevasse depth is widely considered to be a first-order control on calving rate
32 and with terminus position is ultimately a function of ice velocity, strain rate, ice thickness
33 and water depth. The crevasse-depth model has been extended to include the sensitivity of
34 calving rate to a depth of water in surface crevasses^{11, 12, 13} and also the propagation of basal
35 crevasses⁵. These advances have enabled the modelling of individual calving events¹³ as well

36 as the development of models that use assumed realistic and fully dynamic marine boundary
37 conditions for forecasting of sea-level contributions⁴. However, due in large part to a lack of
38 quantitative observational data, the true mechanisms of calving are still largely unknown and
39 thus the development of a universal calving law remains unsolved.

40 Our high temporal and spatial resolution time series of DEMs of the Helheim calving margin
41 (Figure S1) using stereo, terrestrial time-lapse photography (see Methods Section, Terrestrial
42 and ASTER Photogrammetry) gives a detailed account of the evolution of the glacier
43 terminus here presented in 24 hour time-steps. In 2010, Helheim experienced four major
44 calving events between 11 and 30 July with a cumulative areal loss of $\sim 5.06 \text{ km}^2$ ($\sim 8.0 \text{ km}^2$
45 extrapolated to include the area outside the camera view) (Figure 1). At this time, we have
46 not generated volume estimates of the calving events due to the high uncertainty and lack of
47 data coverage in available bed data sets^{14, 15}.

48 The daily evolution of the calving front is shown in longitudinal profiles along the main
49 flowline of the glacier (Figure 2). The most striking feature (Figure 2a) is the large surface
50 depression some 20-30 m in depth running parallel to and about 1.5 km up-glacier from the
51 11 July calving front. This depression developed over the weeks preceding calving during a
52 period of no major calving activity as evidenced from June and early July 2010 stereo
53 ASTER imagery. Depressions like this have been reported previously in the literature and
54 have been attributed to dynamic thinning associated with glacier retreat down a reverse bed
55 slope^{10, 16}.

56 On the first day of the time series, the front advanced ($\sim 22 \text{ m}$) and lifted ($\sim 5 \text{ m}$) and the
57 depression advected downstream at approximately the speed of ice flow (Figure 2a). The
58 glacier then experienced three significant calving events in close succession resulting in the
59 glacier front retreating to the lowest point of the depression. The first of these calving events

60 was captured in high resolution 10 second time-lapse imagery, which shows the formation of
61 a backward-rotating iceberg measuring >4 km across-glacier and 300 m in the direction of
62 glacier flow (Movie S2). Over the next 14 days (Figure 2b) the terminus advanced daily
63 without calving during which time the ice surface lifted at the calving front, slowly at first,
64 accelerating vertically (from 0 to $\sim 8 \text{ m day}^{-1}$) as the next calving event approached. Most
65 noticeably towards the end of the time series, the surface again became depressed to a depth
66 of $\sim 20 \text{ m}$ below the height of the calving front and about 400 m up glacier from the terminus.
67 Note the images show that the depression was not the result of an expanding rift(s) but rather
68 the downward flexure of the surface coupled with the lifting front; evidence that the front
69 section down-glacier of the depression was under rotation. On the last day of the time series,
70 the fourth calving event occurred with the front again retreating to the low point of the
71 depression.

72 We applied feature tracking to the daily images prior to the 12 July 2010 calving event to
73 show glacier displacement along the image-space vertical axis (y_i) as an approximation of
74 actual vertical displacement of the glacier front (see Methods Section, Feature Tracking). The
75 results show the vertical displacement in the longitudinal profiles occurred across the entire
76 visible calving front (Figure 3). The lifting of the front and formation of the associated up-
77 glacier depression are clearly discernible in the imagery days before the iceberg finally
78 detaches. The profiles show that the rotation of the front section accelerated as the calving
79 event neared and ultimately lead to ice failure and calving. Poor lighting prior to the 29 July
80 2010 calving event prohibited their use in feature tracking, however the same mechanism of
81 calving (rotation of the calving section) was also visible in these images.

82 An 11 day time series of topographic data from 2011 (Figure 2c) shows a thinner calving
83 front advanced beyond the location of the 2010 depression with no sign of similar lifting of
84 the calving front or any associated depression. Together with the observed advection of the

85 depression in 2010, this suggests it is unlikely that a bed feature was responsible for the
86 upward displacement of the surface at this location in 2010. Feature tracking applied to the
87 images leading up to the four major 2011 calving events reveals that the same rotation of the
88 glacier's front section preceded calving suggesting that the same style of calving dominated
89 2011's summer dynamic mass loss (Figure S3-Figure S5).

90 To put these results in a longer-term context we took profiles from DEMs generated using the
91 11 year ASTER record (2001 – 2012) (see Methods Section, Terrestrial and ASTER
92 Photogrammetry), which show that the paired frontal lift and surface depression are common
93 at Helheim (Figure 4). These lifted front sections occur at a multitude of positions in the fjord
94 rather than in the same location. The 18 July 2004 ASTER scene captured a clearly rotated
95 front section with the normally vertical calving face clearly visible in the satellite image due
96 to its high rotation angle as the next calving event neared (Figure S6).

97 Our observations suggest that dynamic thinning over a bed depression is not driving these
98 large calving events given: (i) the paired lifting/depression of the front section; (ii) the
99 occurrence at multiple locations in the fjord; and (iii) the clear rotation of the calving section
100 in the feature-tracked images. Similarly, the imagery shows no evidence of longitudinal
101 stretching and widening of surface crevasses until after the surface depressions have
102 collapsed making this mechanism unlikely to be the first-order control on dynamic mass loss
103 at Helheim as often assumed in models. Thus, we also question the significance of the role of
104 water-filled crevasses on dynamic mass loss at Helheim at least during the summers of 2010
105 and 2011. Our observations suggest it is unlikely that these calving events are driven by
106 surface processes. While dynamic thinning and surface crevasses no doubt play an important
107 role in calving dynamics, we conclude that the dominant mechanism of dynamic mass loss at
108 Helheim during the 2010 and 2011 summer season was flexure due to buoyancy-induced
109 rotation.

110 There is considerable literature on buoyancy-induced rotation at marine and lacustrine
111 termini (see ref. 17). Buoyancy forces result when the terminal surface is lowered relative to
112 water height causing an otherwise grounded glacier to thin, becoming increasingly out of
113 buoyant equilibrium. As buoyancy forces increase the ice must rotate to restore equilibrium
114 either slowly by creep or rapidly by fracture propagation¹⁷. This mechanism is consistent with
115 our observations and thus we consider potential causes of increasing buoyant flexure at
116 Helheim's terminus.

117 In order for buoyancy to cause the events we have observed, the ice must be lowered relative
118 to water height. Previous studies have reported that increasing buoyancy results when surface
119 ablation causes ice to thin below flotation¹⁸. Recent models estimate an average summer
120 ablation of $\sim 0.055 \text{ m d}^{-1}$ at Helheim's calving margin¹⁹. While this is small, buoyancy is
121 believed to be insufficient for rotating large, full-glacier-thickness icebergs unless the calving
122 portion of the glacier is near flotation²⁰. Therefore, even small changes in surface elevation
123 may be significant. However, we find that given the high flow speed of the glacier at the
124 calving margin ($>20 \text{ m d}^{-1}$), the daily evolution of the calving front observed between two
125 backward-rotating calving events (Figure 2b) is consistent with the glacier being driven
126 below flotation into deeper water at a rate faster than it can adjust. A similar phenomenon has
127 been seen downstream of the grounding line of ice shelves (e.g. ref. 21). Figure 5 presents a
128 schematic of our interpretation of the calving we have observed at Helheim. While the role of
129 bottom crevasses is unknown, it has been suggested that they are likely to form in areas of
130 high longitudinal strain rates and low basal effective pressure²² as would be expected at
131 Helheim's calving front.

132 The majority of calving events we observed at Helheim produced overturning icebergs.
133 Atypically, the full width event on 12 Aug 2011 (Figure S5) produced an overturning iceberg
134 on the south side of the fjord where the calving section width-to-height ratio (ϵ) was small

135 and a tabular iceberg on the north side where ε was considerably larger. While frontal uplift
136 was only seen on the south side, a depression was visible across the calving width though
137 significantly less pronounced on the north side. The factors controlling ε here, shown to be
138 key in determining the style of calving²⁰, are unknown but likely involve a complex interplay
139 between the factors described in Figure 5 and in particular the effects of subglacial discharge
140 and fjord circulation on subaqueous melting. This may be key in providing an link between
141 calving behaviour and fjord temperatures/circulation²³ and an explanation of any seasonal
142 variation in calving style and rate that is more consistent with observations than seasonal
143 water in crevasses.

144 Understanding the mechanisms behind large calving events is vital for producing reliable
145 models to forecast Greenland's future contribution to sea-level. Models typically reproduce
146 observed glacier behaviour over relatively short time-scales which may be insufficient for
147 extrapolation into the future if not based on the real physical processes. We provide improved
148 observations of calving during two summers at Helheim Glacier providing a detailed
149 characterisation of typical large calving events. Our results show that large, overturning
150 icebergs begin rotating visibly several days before detachment from the glacier under
151 buoyancy forces characterised by a paired lifting and depression of the calving section. Our
152 results suggests that treatment of the calving criterion based on the penetration of air and
153 water-filled surface crevasses to the waterline, which has previously been used as a first-order
154 approximation of calving^{11, 13}, is missing key elements of calving dynamics and could
155 misrepresent dynamic mass-loss from the ice sheet. However, factors controlling the style
156 and rate of calving, especially bathymetry, fjord temperatures and circulation (and their
157 effects on subaqueous melting) are unknown and it is likely that the primary control on
158 calving changes over time. Our research highlights the many unknowns that persist about the
159 drivers of calving and further work that needs to be undertaken.

160 **Methods**

161 Helheim Glacier is a major outlet of the Greenland Ice Sheet draining an area of ~52,000
162 km². Its recent behaviour has been under much scrutiny due to reports of acceleration^{2, 24, 25},
163 retreat^{25, 26, 27} and thinning^{25, 26} found to occur quasi-synchronously with other marine-
164 terminating glaciers in the southeast^{25, 28}. As the calving front is the closest major outlet
165 glacier to southeast Greenland's main settlement, Tasiilaq, Helheim has been a primary target
166 of data collection efforts over the last decade.

167 **Terrestrial and ASTER Photogrammetry.** In the summers of 2010 and 2011, we installed
168 two 15.1 megapixel Canon 50D digital single-lens reflex (DSLR) cameras on the south shore
169 of Helheim Fjord ~300 m apart and ~3.5 km down-fjord from the 2010 calving front (Figure
170 1). We used fixed 28 mm focal length lenses, which are sufficiently wide-angle to capture the
171 majority of the glacier terminus without needing to be too far away thereby maximising
172 image detail but with minimal distortion. Camera viewsheds and the area of image overlap
173 enabling the extraction of elevation models are shown in Figure 1. The camera clocks were
174 manually synchronised and set to take an image every 60 minutes, 24 hours a day. Clock drift
175 was <15 seconds over a period of several months. In 2010, the cameras were powered with
176 internal batteries, which provided hourly collection between 11 to 30 July (20 days, ~500
177 images). In 2011, 11 days of stereo imagery were collected from 27 June to 08 July due to a
178 power failure in one camera but mono imagery was collected to 29 August.

179 Daily DEMs were generated using images taken at 0830 UTC due to optimal lighting of the
180 calving front. Camera calibration was used to model and minimise focal length and lens
181 distortion errors. Ground control points (GCPs), which link 2D image space to 3D ground
182 space were extracted from stable areas of 2007 lidar DEMs following the methodology in ref.
183 29. DEMs were produced from stereo imagery using the 3D viewing capabilities of the

184 SOCET SET digital photogrammetry suite which is key for pinpointing the location of the
185 GCP in the images. The photogrammetric bundle adjustment and DEM extraction was
186 carried out in Topcon's ImageMaster.

187 DEMs were extracted nominally on a 5 m grid, where image resolution permitted since, with
188 oblique imagery, image resolution decreases with distance from the cameras. These factors as
189 well as the complicated surface topography meant the resulting topographic model took the
190 form of an irregular cloud of xyz coordinate triplets with a maximum resolution of 5 m but
191 that dropped with increasing distance from the camera. To simplify processing, the point
192 clouds were interpolated to a regular 10 m grid using a local polynomial approach that
193 assigns values on the grid using a weighted least squares fit to data within a user specified
194 search window of 50 m. This window size was found to preserve sufficient surface detail for
195 comparison while eliminating higher frequency elevation variations. An example of the
196 resulting DEMs is given in Fig. S1.

197 The quality of DEMs of a dynamic surface like the calving margin of Helheim Glacier is
198 difficult to quantify. For the terrestrial imagery, the photogrammetric block adjustment uses
199 measured points and camera calibration information to predict the location and attitude of the
200 cameras whose positions were surveyed with differential global positioning system data
201 (DGPS) yielding an indication of the quality of the image block adjustment. The root mean
202 square error (RMSE) of the predicted camera positions (Table S1) were sub-2m in XY and
203 sub-metre in Z indicating a high relative accuracy between DEMs. Comparison to DGPS
204 camera positions give the absolute accuracy of the DEMs. Typically, error due to the image
205 correlation stage of DEM generation is evaluated by comparing the data to a ground truth
206 data set, which is of course not available here. Therefore, we conservatively estimate the
207 error of our DEMs at ± 1 m in the vertical and ± 5 m horizontal at the calving front (both
208 degrading with distance from the cameras). We base these estimates on the block adjustment

209 results and the ability of our DEMs to easily resolve the daily flow of the glacier which is
210 expected to be $\sim 20 \text{ m day}^{-1}$.

211 We produced DEMs from stereo ASTER imagery at 50 m resolution using the ASTER sensor
212 model of BAE Systems Socet SET digital photogrammetry suite. While it is theoretically
213 possible to produce ASTER DEMs at the same resolution as the imagery (15 m), the quality
214 control of such a large and dense data set on such an irregular surface is difficult and
215 unnecessary for characterising the important changes at Helheim. Similarly to the terrestrial
216 photographs, ground control points were extracted from the 2007 lidar DEM. The processing
217 of the imagery was carried out entirely in Socet Set where the software's 3D viewing
218 capabilities enabled the accurate measurement of ground control points in the image plane.
219 The average root mean square error (RMSE) of the photogrammetric block adjustment was
220 5.2 m in X, 5.2 m in Y and 1.1 m in Z suggesting a good fit of the sensor model to the image
221 measurements. Due to low resolution of ASTER imagery (15 m) the quality of the resulting
222 DEM will be lower than the RMSE of the model fit to image measurements. Quality will also
223 be negatively affected by poor image contrast on dark and bright surfaces. We estimate
224 planimetric error to be $\pm 8 \text{ m}$ and elevation error in the ASTER DEMs to be $\pm 2.5 \text{ m}$.

225 **Feature Tracking.** There is a large amount of spatial information recorded in photographic
226 time series that becomes evident when manually 'flicking' through a data set. To provide a
227 simple means of quantifying the evolution of the Helheim calving front as captured in our
228 time series, we used the California Institute of Technology's COSI-Corr orthorectification
229 and feature tracking module created for integration in the ENVI environment³⁰. COSI-Corr
230 was developed primarily for satellite and airborne images (i.e. near vertical or nadir viewing
231 angle) and typically, images are orthorectified prior to image correlation to provide
232 displacements in ground coordinates. The orthorectification of high oblique imagery (i.e.
233 where the horizon is visible) is difficult and was unnecessary for demonstrating the

234 movement of the ice at the calving front. COSI-Corr outputs the x and y components of
235 displacement in image space (x_i , y_i). In this image configuration, ice displacement at the
236 calving front due to glacier flow is dominantly along the x_i image axis. Therefore, we
237 approximate vertical ice displacement using movement along the y_i axis. This assumption
238 degrades towards the left side of the image where there is a larger component of glacier flow
239 along the y_i axis, but the rotation of the front section remains clearly visible. Displacement
240 measured on the stationary mountains suggests that the errors in these figures is ~ 1 pixel.

241 **Acknowledgements**

242 TDJ was supported by The Leverhulme Trust GLIMPSE Project (F/00391/J) and the Climate
243 Consortium for Wales (C3W). NS and KS were also supported by The Leverhulme Trust.
244 Field work was funded by The Leverhulme Trust, a Royal Geographical Society EPSRC
245 Geographical Research Grant (20IGC 01/10), NERC (NE/I007148/1) and the European
246 Union Seventh Framework Programme [FP7/2007-2013] under grant agreement n° 262693
247 [INTERACT]. ASTER imagery were acquired through NASA's Land Processes Distributed
248 Active Archive Center (LP DAAC) with thanks to Operation IceBridge and Bill Krabill. The
249 authors would also like to acknowledge software support from Nick Russill at TerraDat
250 Geophysics (Image Master) and François Ayoub (COSI-corr). We acknowledge the use of
251 bed DEM from CReSIS generated with support from NSF grant ANT-0424589 and NASA
252 grant NNX10AT68G.

253 **Author Contributions**

254 TDJ developed the methodology, undertook the analysis and interpretation and wrote the
255 manuscript. TM was the grant-holder and contributed to data collection and interpretation.

256 NS and KS contributed to methodological development and data collection. MO contributed
257 to the interpretation. All authors contributed to the manuscript preparation.

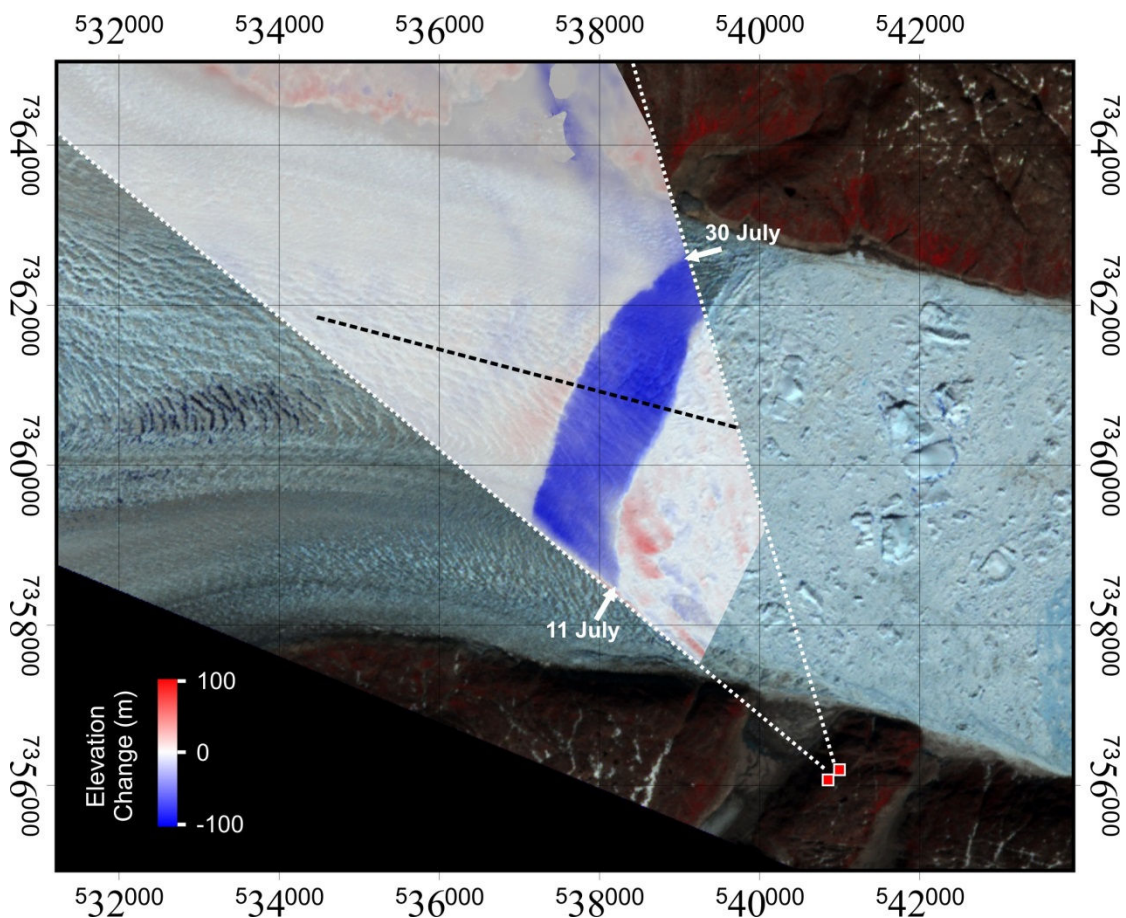
258 **References**

- 259 1. Hagen J. O., Kohler J., Melvold K. & Winther J. G. Glaciers in Svalbard: mass
260 balance, runoff and freshwater flux. *Polar Res.* **22**, 145-159 (2003).
- 261 2. Rignot E. & Kanagaratnam P. Changes in the velocity structure of the Greenland
262 ice sheet. *Science* **311**, 986-990 (2006).
- 263 3. van der Veen C. J. Calving glaciers. *Prog. Phys. Geog.* **26**, 96-122 (2002).
- 264 4. Nick F. M., Vieli A., Andersen M. L., Joughin I., Payne A., Edwards T. L., *et al.*
265 Future sea-level rise from Greenland's main outlet glaciers in a warming climate.
266 *Nature* **497**, 235-238 (2013).
- 267 5. Nick F. M., van der Veen C. J., Vieli A. & Benn D. I. A physically based calving
268 model applied to marine outlet glaciers and implications for the glacier dynamics.
269 *J. Glaciol.* **56**, 781-794 (2010).
- 270 6. Meier M. F. & Post A. Fast tidewater glaciers. *J. Geophys. Res.* **92**, 9051-9058
271 (1987).
- 272 7. Pfeffer W. T., Dyurgerov M., Kaplan M., Dwyer J., Sassolas C., Jennings A., *et*
273 *al.* Numerical modeling of Late Glacial Laurentide advance of ice across Hudson
274 Strait: Insights into terrestrial and marine geology, mass balance, and calving
275 flux. *Paleoceanography* **12**, 97-110 (1997).
- 276 8. van der Veen C. J. Tidewater calving. *J. Glaciol.* **42**, 375-385 (1996).
- 277 9. Vieli A., Funk M. & Blatter H. Flow dynamics of tidewater glaciers: a numerical
278 modelling approach. *J. Glaciol.* **47**, 595-606 (2001).
- 279 10. Vieli A., Jania J. & Kolondra L. The retreat of a tidewater glacier: observations
280 and model calculations on Hansbreen, Spitsbergen. *J. Glaciol.* **48**, 592-600
281 (2002).
- 282 11. Benn D. I., Hulton N. R. J. & Mottram R. H. 'Calving laws', 'sliding laws' and the
283 stability of tidewater glaciers. *Ann. Glaciol.* **46**, 123-130 (2007).
- 284 12. Vieli A. & Nick F. M. Understanding and modelling rapid dynamic changes of
285 tidewater outlet glaciers: issues and implications. *Surv. Geophys.* **32**, 437-458
286 (2011).

- 287 13. Cook S., Zwinger T., Rutt I. C., O'Neel S. & Murray T. Testing the effect of water
288 in crevasses on a physically based calving model. *Ann. Glaciol.* **53**, 90-96 (2012).
- 289 14. Gogineni P. CReSIS Radar Depth Sounder Data, Lawrence, Kansas, USA. Digital
290 Media. <http://data.cresis.ku.edu/>. 2012.
- 291 15. Bamber J. L., Griggs J. A., Hurkmans R. T. W. L., Dowdeswell J. A., Gogineni S.
292 P., Howat I., *et al.* A new bed elevation data set for Greenland. *The Cryosphere* **7**,
293 499-510 (2013).
- 294 16. Joughin I., Howat I., Alley R. B., Ekstrom G., Fahnestock M., Moon T., *et al.* Ice-
295 front variation and tidewater behavior on Helheim and Kangerdlugssuaq Glaciers,
296 Greenland. *J. Geophys. Res.* **113**, F01004 (2008).
- 297 17. Benn D. I., Warren C. R. & Mottram R. H. Calving processes and the dynamics of
298 calving glaciers. *Earth-Sci. Rev.* **82**, 143-179 (2007).
- 299 18. Howarth P. J. & Price R. J. The proglacial lake of Breiðamerkurjökull and
300 Fjallsjökull, Iceland. *Geogr. J.* **135**, 573-581 (1969).
- 301 19. Andersen M. L., Larsen T. B., Nettles M., Elosegui P., van As D., Hamilton G. S.,
302 *et al.* Spatial and temporal melt variability at Helheim Glacier, East Greenland,
303 and its effect on ice dynamics. *J. Geophys. Res.-Earth* **115**, (2010).
- 304 20. Amundson J. M., Fahnestock M., Truffer M., Brown J., Luthi M. P. & Motyka R.
305 J. Ice mélange dynamics and implications for terminus stability, Jakobshavn
306 Isbrae Greenland. *J. Geophys. Res.-Earth* **115**, (2010).
- 307 21. Vaughan D. G. Tidal flexure at ice shelf margins. *J. Geophys. Res.* **100**, 6213-
308 6224 (1995).
- 309 22. Van der Veen C. J. Fracture mechanics approach to penetration of bottom
310 crevasses on glaciers. *Cold Reg. Sci. Technol.* **27**, 213-223 (1998).
- 311 23. O'Leary M. & Christoffersen P. Calving on tidewater glaciers amplified by
312 submarine frontal melting. *The Cryosphere* **7**, 119-128 (2012).
- 313 24. Luckman A., Murray T., de Lange R. & Hanna E. Rapid and synchronous ice-
314 dynamic changes in East Greenland. *Geophys. Res. Lett.* **33**, L03503, doi:
315 03510.01029/02005GL025428 (2006).
- 316 25. Howat I. M., Joughin I., Fahnestock M., Smith B. E. & Scambos T. A.
317 Synchronous retreat and acceleration of southeast Greenland outlet glaciers 2000-
318 06: ice dynamics and coupling to climate. *J. Glaciol.* **54**, 646-660 (2008).

- 319 26. Howat I. M., Joughin I. & Scambos T. A. Rapid changes in ice discharge from
320 Greenland outlet glaciers. *Science* **315**, 1559-1561 (2007).
- 321 27. Moon T. & Joughin I. Changes in ice front position on Greenland's outlet glaciers
322 from 1992 to 2007. *J. Geophys. Res.-Earth* **113**, (2008).
- 323 28. Murray T., Scharrer K., James T. D., Dye S. R., Hanna E., Booth A. D., *et al.*
324 Ocean regulation of glacier dynamics in south-east Greenland and implications
325 for ice-sheet mass changes. *J. Geophys. Res.-Earth* **115**, doi:
326 10.1029/2009JF001522 (2010).
- 327 29. James T. D., Murray T., Barrand N. E. & Barr S. L. Extracting photogrammetric
328 ground control from lidar DEMs for change detection. *Photogramm. Rec.* **21**,
329 310-326 (2006).
- 330 30. Ayoub F., Leprince S. & Avouac J. P. Co-registration and correlation of aerial
331 photographs for ground deformation measurements. *ISPRS J. Photogramm.* **64**,
332 551-560 (2009).
- 333
- 334

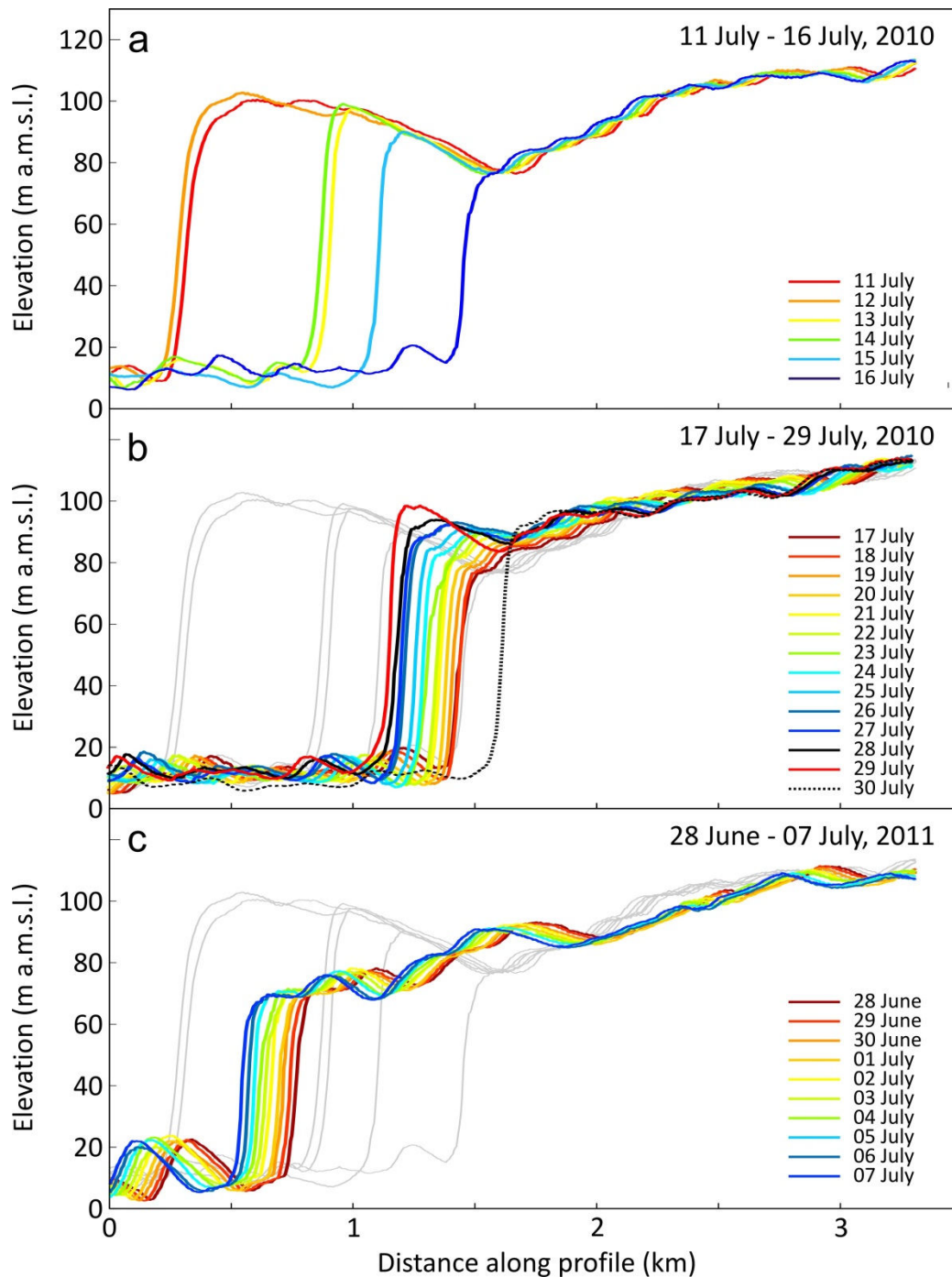
335 **Figures**



336

337 **Figure 1 | Camera location with differenced DEM.** Camera stations on the south side of
338 Helheim Fjord are shown on this 08 July 2010 ASTER false colour composite orthoimage.
339 Approximate stereo view-shed of the cameras is shown and the location of the profiles in
340 Figure 2. Elevation changes at Helheim from 11 to 30 July, 2010 (front positions indicated)
341 are overlaid showing ice loss of $\sim 4.0 \text{ km}^2$ in the cameras' view-shed and $\sim 0.29 \text{ km}^3$ above
342 sea-level volume loss. Negative change anomaly in the top right of overlay are errors
343 associated with a mountain shadow. Large elevation changes in the ice mélange show the
344 movement of icebergs in the fjord and the production of new icebergs by the calving events.

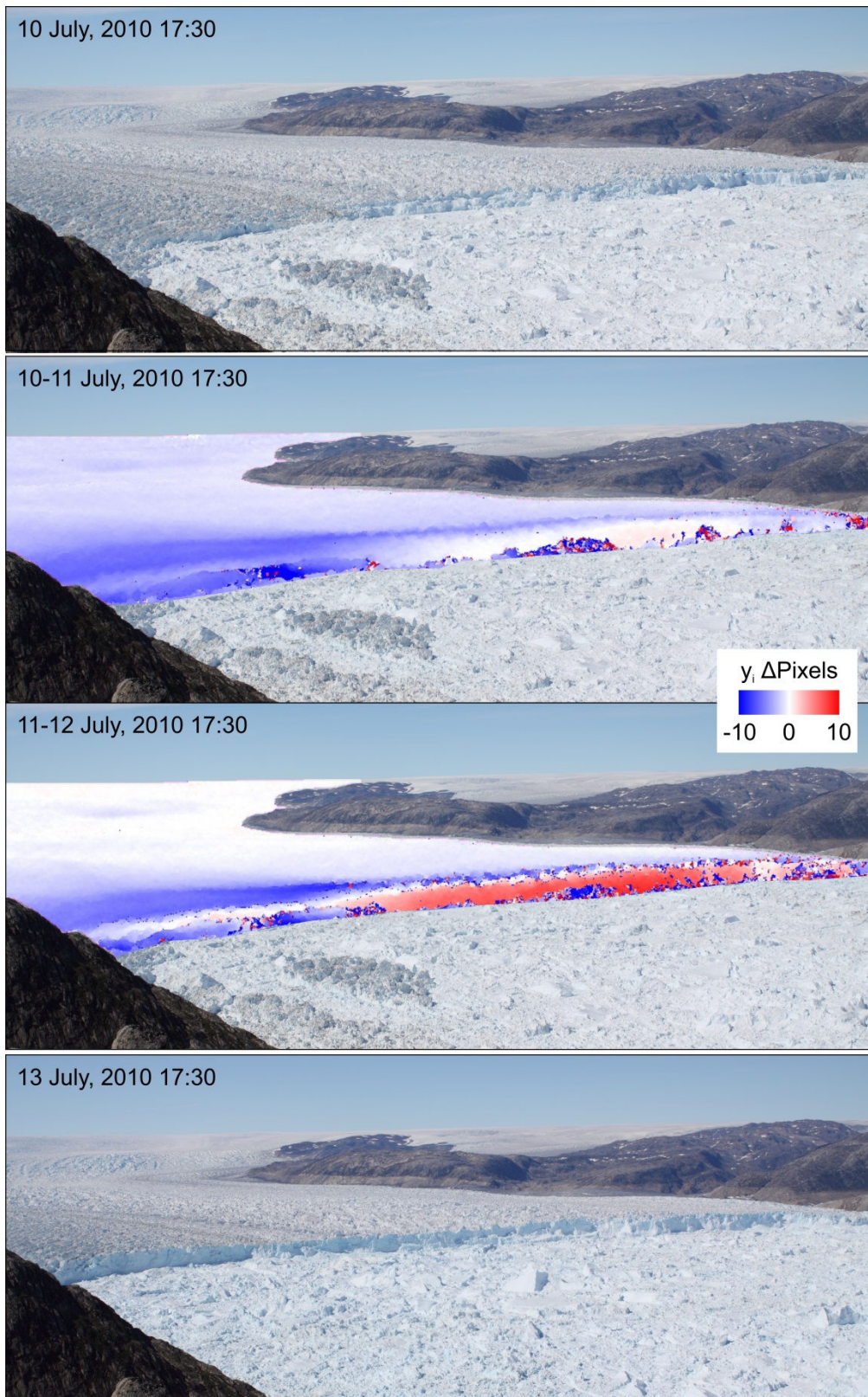
345



346

347 **Figure 2 | Longitudinal elevation profiles on Helheim central flow line derived from**
 348 **stereo terrestrial photographs.** Location of profiles is shown in Figure 1. (a) In the first six
 349 days of the time series the glacier terminus experienced three significant calving events
 350 causing the front to retreat to a pre-existing depression which the ASTER record shows had
 351 been deepening over the preceding period of minimal frontal activity. (b) With the profiles
 352 from (a) in the background, over the next 14 days, as the terminus advanced daily, the front

353 lifted again forming a depression to which the front retreats on the last day of the time series.
354 (c) In 2011, the front passes over the area of the 2010 depression without any sign of a
355 similar surface low. As a guide, our error estimates for these profiles are about \pm the line
356 width. Elevations are above mean seal level (a.m.s.l.)



357

358 **Figure 3 | Image feature tracking prior to the 12 July 2010 18:30 UTC calving event.**

359 This event was a full-width and full-depth calving event and was captured in 10 second time-

360 lapse (see Movie S2). We applied feature tracking methods to the imagery over two 24 hour

361 periods prior to the calving event to show displacement at the calving front. Displacement
362 units are in pixels of displacement in image space (along y_i axis) with positive up,
363 approximating vertical movement in real space.

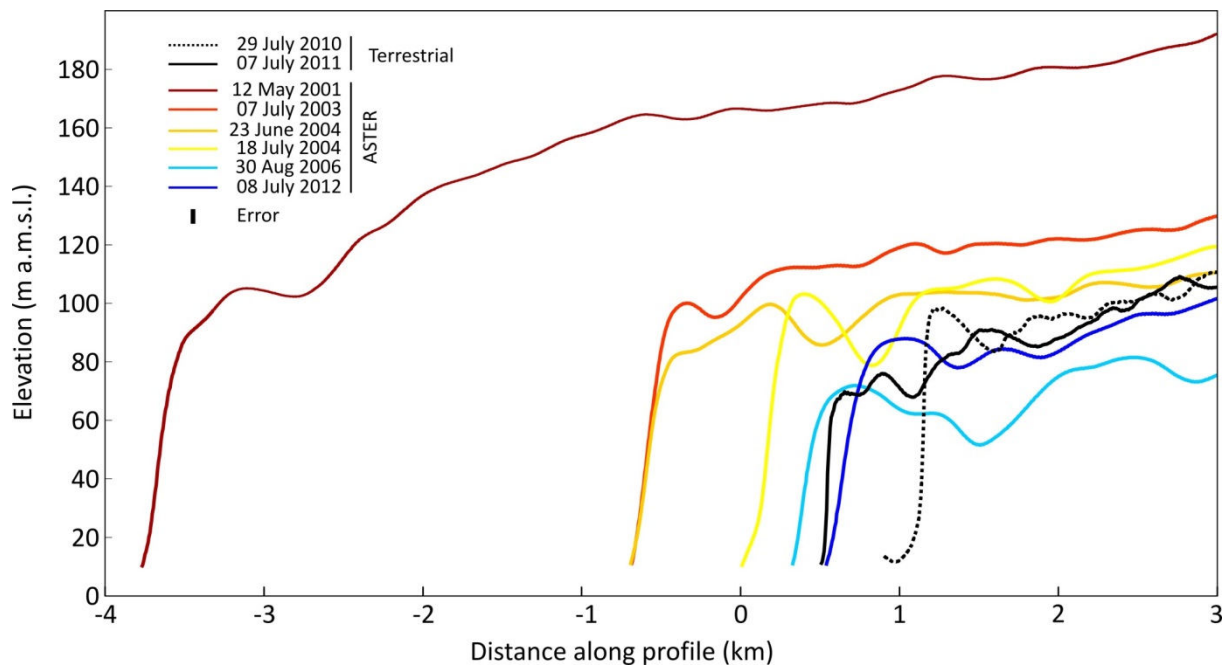


Figure 4 | 2010 and 2011 calving front in the context of 11 years of the ASTER record.

Profiles derived from the terrestrial imagery for the beginning of both the 2010 and 2011 time series are shown.

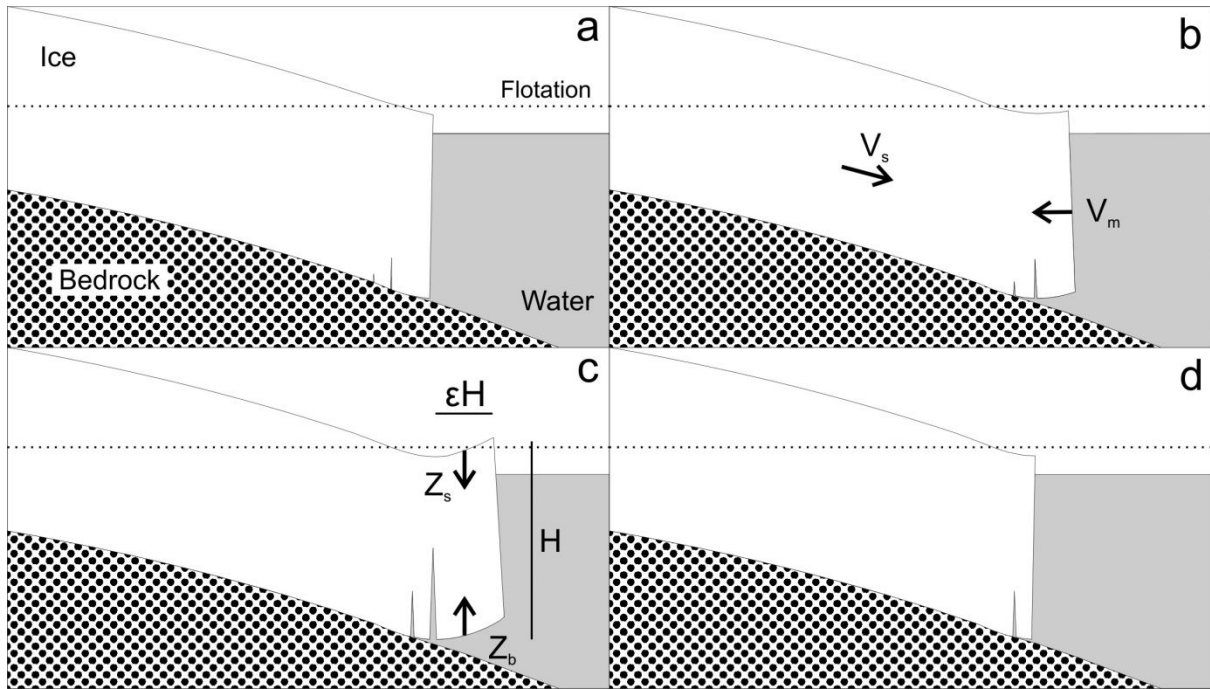


Figure 5 | Schematic of proposed calving by buoyant flexure. (a) The forward motion of the glacier drives the front section below flotation as it moves into deeper water. Note the likely presence of basal crevassing. (b) The ice initially responds to increasing buoyancy primarily by creep as indicated by the slow initial response of the calving front (17 – 28 July, Figure 2b). The bed slope, surface slope, ice velocity (V_s) and frontal subaqueous melting (V_m) will contribute to controlling the rate at which buoyancy increases. (c) In the days immediately prior to calving (28 – 29 July, Figure 2b) the rate of rotation increases dramatically, suggesting the propagation of a bottom crevasse(s), with rapid lifting of the front and depression of the surface at the hinge point of calving (likely at or near the grounding line). The dimensions of the calving section, ϵH and H , will in part be determined by a balance between surface (Z_s), basal (Z_b) and frontal subaqueous melting. (d) Finally, the buoyancy forces overcome the strength of the remaining intact ice and the ice eventually fails suddenly at the hinge point of the depression (29-30 July, Figure 2b).